Influence of membrane wing active deformation on the aerodynamic performance of an aircraft model

FENG SiYuan, GUO QinFeng, WANG JinJun[*] & XU Yang

Fluid Mechanics Key Laboratory of Education Ministry, Beijing University of Aeronautics and Astronautics, Beijing 100191, China

The aerodynamic performance of a simplified aircraft model with a pair of actively deformed membrane wings is investigated experimentally in this work. The active deformation is achieved with Macro fiber composite (MFC) actuators, which are attached to the upper surface of the wings and occupied 13.7% of the wing surface area. Wind tunnel experiments are conducted to evaluate the influence of membrane active deformation on the aerodynamic performance of the aircraft. The results show that the membrane deforms and vibrates under the actuation which can effectively suppress the leading-edge separation and facilitate the reattachment. Therefore, compared with the rigid wing model, the lift coefficient of the actively deformed membrane wing model is enhanced remarkably from the angle of attack of 7° to 22°. The stall angle is delayed by 2°, and a maximum lift coefficient enhancement of 32.5% is reached, which shows a wide potential application in improving the aerodynamic performance of modern aircraft.

fluid-structure interaction, flexible membrane wing, active control, force measurement, flow field measurement

1 Introduction

Micro-air vehicles (MAVs) with small physical dimensions and low flight speeds have attracted substantial attention for the broad prospect of military and civilian applications in the last few decades [1]. However, the low Reynolds number (10^4–10^5) flow regime is often accompanied by laminar boundary layer separation and low lift-to-drag ratio, resulting in degraded aerodynamic performance [2]. Therefore, promoting the aerodynamic performance of MAVs is a significant work with difficulties.

Employing flexible membrane wings is one of the chief means to optimize the aerodynamic performance of MAVs. The passive static deformation of membrane wings has been shown to improve the lift-to-drag ratio and delay stall at low Reynolds number in earlier studies [3,4]. The adaptability of flexible wings in the unsteady flight environment was also shown [5]. Subsequently, the vibration of the membrane was also observed [6], and it was confirmed later that this vibration could suppress flow separation by exciting the shear layer [7]. Based on the flow-induced vibration, membrane wing has potential for energy harvesting as well [8].

The fluid-structure interaction of two-dimensional or rectangular membrane wings has been focused on first. Song et al. [8] measured the static and dynamic deformations of membrane wings. The relationship between the membrane camber and the Weber number that compares the aerodynamic load to the membrane elasticity was presented. Meanwhile, the close connection between the membrane vibration with the free eigenmodes of the membrane and the Strouhal number was pointed out. Moreover, Rojratsirikul et al. [10] suggested the dependence of the membrane vibration on the relative location and the magnitude of the unsteadiness of the separated shear layer. He and Wang [11]

studied the spectrum of the membrane vibration and flow field. It was found that membrane wing vibration and flow field were strongly coupled. In addition, the effects of aspect ratio on fluid-structure interactions of membrane wings were investigated by Bleischwitz et al. [12]. The significant impact of aspect ratio on deflections along the span and chordwise vibration modes was observed, thus affecting aerodynamic forces.

Besides, for the application of membrane wings on MAVs with possibly more complex configurations, studies on three-dimensional aircraft models with membrane wings have been conducted as well. In the investigation of Béguin et al. [13,14], a semi-span model with a morphing membrane wing was adopted, and it was found that the deformation of the membrane could be influenced by changing the planform geometry and membrane pre-stress. Thereby, aerodynamic performance improvement could be obtained over a broader scope of flow conditions. Guo et al. [15] measured the force, membrane deformation, and velocity field of an aircraft model with membrane wings. It was proved that the vibration of the membrane led to stronger mixing near the upper wing surface, thereby suppressing the flow separation. Besides, the leading-edge separated flow could be weakened or re-attached in a range of angles of attack.

Because the membrane deformation, as well as the resulting aerodynamic performance improvement, are sensitive to a variety of factors, the effect of membrane passive deformation may be unsatisfactory in some cases. Thus, active control for the deformation of membrane wings is one of the ways to improve its performance further. Hays et al. [16] used the dielectric elastomer, the compliance of which could be changed actively, on an elliptical membrane wing. Thus, suitable membrane tension could be obtained under electrostatic fields, resulting in adjusted membrane deformation under aerodynamic loads as well as optimized aerodynamic performance. Curet et al. [17] used the same material on a rectangular membrane wing. It was shown that when the wing was forced with an oscillating field at specific frequencies, the excitation of the membrane kinematics and the increment of its mean camber could enhance lift coefficient and delay stall significantly. In the following work, Bohnker and Breuer [18] measured the membrane kinematics and flow field, and the correlation between lift enhancement and instabilities in the separated flow was revealed.

Another method of active control on membrane wings was employed in this work. Macro fiber composite (MFC) actuator, a smart piezoelectric material with potential for active flow control [19,20], was used to produce active deformation on membrane wings of a simplified aircraft model directly. The influence of the membrane deformation on the aerodynamic performance was evaluated by force measurement. Furthermore, the velocity field was measured and the me-chanism behind the aerodynamic performance improvement was revealed.

2 Experimental setup

The experiment was conducted in the open circulation low-speed wind tunnel D1 at Fluid Mechanics Key Laboratory of Education Ministry, Beijing University of Aeronautics and Astronautics. This wind tunnel has a 1.45 m long oval test section with a 1.02 m×0.76 m inlet and a 1.07 m×0.82 m outlet. The maximum free stream velocity is 50 m/s, and the experimental free stream velocity is fixed at 20 m/s with a turbulent intensity of less than 0.3% and a free flow deflection angle of less than 0.1° in this investigation.

2.1 Experimental model

A simplified aircraft model with a pair of actively deformed membrane wings has been adopted for the experiment, as shown in Figure 1. The configuration references the work of Guo et al. [15], which is a simplified transport category airplane model, with some modifications on the wing. The fuselage has a total length of 219.3 mm, and a diameter of 40 mm. The axial section of the nose is elliptical. Besides, the leading-edge sweep angle of the wing is 15°. The wingspan is 269.67 mm, and the length of wing root c_{root} is 44.57 mm. Thus, at the experimental free stream velocity U_∞ of 20 m/s, the Reynolds number based on the length of the wing root is Re_c=6.1×10^4.

The wing is made of aluminum (2A12) with a thickness t of 3 mm, and its leading-edge and trailing-edge are rounded off. Then there is a 2.5-mm deep groove cut from the upper surface, and its edge is 3 mm from the leading-edge and trailing-edge of the wing, for membrane layout. Besides, the wing is lacquered in matte black, for PIV measurement.

The membrane material used in the experiment is thermoplastic polyurethanes (TPU) with a thickness of h=0.05 mm, Young's modulus of E=31.2 MPa, and a density of ρ=1.1 g/cm^3. To simulate the tensioned membrane in practice, the membrane is uniformly stretched by a pre-strain of ε=10% along the chordwise. Then, the membrane is carefully attached to the upper surface of the wings using double-sided tape. Meanwhile, it is reinforced at the leading-edge and trailing-edge using transparent tape. Thus, in this work, membrane tension is dominated by pre-stress. The non-dimensional ratio $\Pi_2 = \left(\dfrac{{}^0 S h}{q_\infty c_{root}} \right)$ (defined by Smith and Shyy [5]) of the pre-stress ${}^0 S$ to the free-stream dynamic pressure q_∞ is 13.5.

MFC actuators (Smart Material M-8557-P1) are attached to carbon fiber plates sizing 36 mm×16 mm×0.2 mm with epoxy. Then the carbon fiber plates are attached to the inside
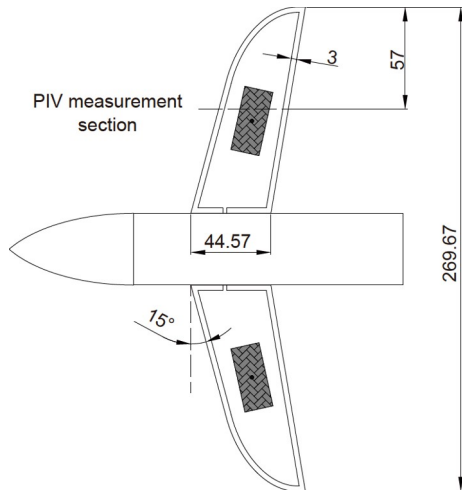
Figure 1 Schematic diagram of simplified aircraft model.

Figure 2 (Color online) Working principle of the actuator.

of the membrane with double-sided tape, fundamentally located at the centroid of the groove. The area ratio of the carbon fiber plate to the wing is 13.7%. The MFC actuators can be expanded and drive the carbon fiber plates to bend when a voltage is applied, as shown in Figure 2.

The actuators used on the pair of wings are connected in parallel. The maximum operational range of the MFC actuators is −500 V to 1500 V. In order to maximize the actuation, the input voltages in the range from −1 V to 3 V, produced by a Tektronix AFG1062 Arbitrary/Function Generator, are amplified by an ATA-7025 High Voltage Amplifier. The resulting actuation signal is as follows:

$$V(t) = \frac{1}{2} V_{pp}[\sin(2\pi f t) + 0.5], \tag{1}$$

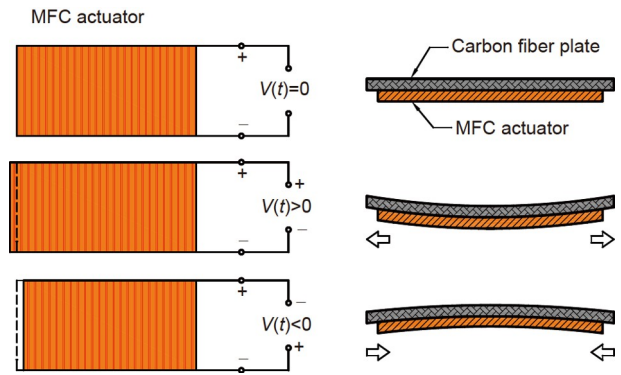where V_{pp} is the peak-to-peak voltage, f is the actuation frequency, and t denotes time.

Controlled wing and uncontrolled wing are used to denote the wing with and without actuation, respectively. For comparison, two other types of wings were also adopted in the experiment: rigid wing, wing only using membrane on the upper surface without actuators (hereafter refer as flexible wing), as shown in Figure 3.

2.2 Experimental equipment and method

2.2.1 Deformation measurement
A laser sensor (Panasonic HL-C203BE) was used in the deformation measurement, which could measure the displacement of a single point on the model. The diffuse reflection mode was adopted in this experiment, while the measurement center distance was 30 mm. The sampling cycle was set to 40 µs, and the measurement range was ±5 mm. The resolution was 0.25 µm, and the linearity was ±0.03% F.S. The deformation measurement was carried out without flow, and the peak-to-peak displacement D_{pp} was
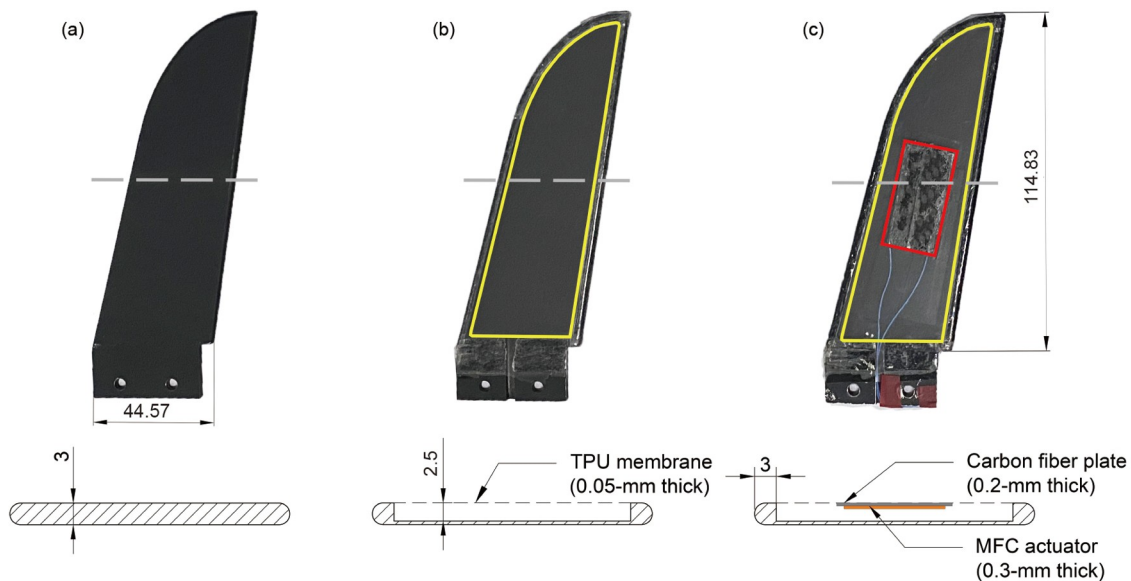

Figure 3 (Color online) Three types of wing models. (a) Rigid wing; (b) flexible wing; (c) flexible wing with actuator.

taken to evaluate the deformation.

2.2.2   Force measurement

A six-component strain balance, which has been used in several studies with good accuracy [15,21,22], was employed for force measurement. The force coefficients were obtained by averaging 20000 sampling points within 20 s. The angle of attack α was controlled by a mechanism varying from 0° to 66° with an accuracy of 0.05°. The interval of α was 1° in the ranges of α=0°–26° and 40°–50°, while the interval of α was 2° in the ranges of α=26°–40° and 50°–66°. The maximum blockage ratio was 2.5% obtained at α=66°, which was negligible because of its low value.

2.2.3   Particle image velocimetry

To reveal the mechanism behind the aerodynamic performance improvement, the flow fields of a section at the wing mid-span location were measured by particle image velocimetry (PIV). This section passed through the actuator. Meanwhile, it has a certain distance from the fuselage and wingtip. Thus, the dominant flow structure can be observed qualitatively by PIV measurement. A Charge-Coupled Device (CCD) camera was used for PIV measurement. The resolution of the CCD camera was 2456×2058 pixels to capture the field of view of about 120 mm×100 mm, resulting in a magnification of 0.05 mm/pixel. The time interval between two straddle frames was 20 µs, and the sampling frequency was 5 Hz. 1000 instantaneous velocity fields were obtained in a single experiment. Meanwhile, every single experiment was repeated three times. A Vlite-380 dual pulse laser was used as a light source. The wavelength was 532 nm, and the pulse power was 380 mJ. Small droplets produced by a fog machine were used as tracer particles with a diameter of about 1 µm. The sketch of the PIV experiment is shown in Figure 4.

Referring to Qu et al. [23], the particle velocity u_p in the PIV measurement was

$$u_p = x_p / t_p, \tag{2}$$

where x_p is the physical displacement of particles between one image pair and t_p is the corresponding time interval. The uncertainty of u_p originating from both the uncertainties of x_p and t_p could be estimated by the uncertainty propagation formula (Kline and McClintock [24]):

$$\varepsilon(u_p) = \sqrt{\left(\frac{\partial u_p}{\partial x_p}\right)^2 \varepsilon^2(x_p) + \left(\frac{\partial u_p}{\partial t_p}\right)^2 \varepsilon^2(t_p)}$$

$$= \sqrt{\left(\frac{1}{t_p}\right)^2 \varepsilon^2(x_p) + \left(-\frac{x_p}{t_p^2}\right)^2 \varepsilon^2(t_p)}, \tag{3}$$

where ε denotes the uncertainties. In this work, t_p was accurately determined by the PIV system, so the item including $\varepsilon(t_p)$ in the equation was negligible. Meanwhile, the max-
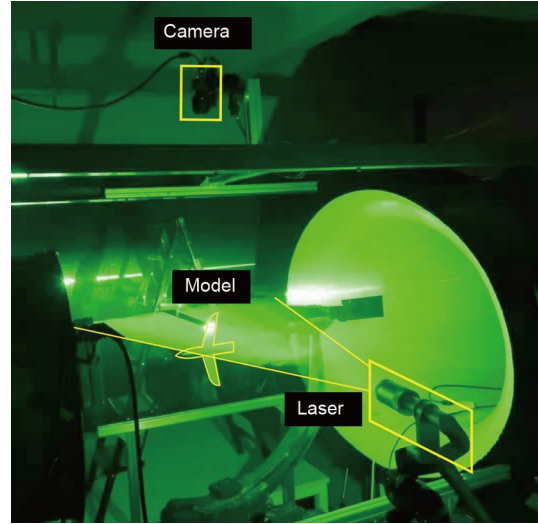

Figure 4   (Color online) Sketch of PIV experiment.

imum uncertainty of the particle displacement was 0.1 pixel, therefore, the corresponding $\varepsilon(x_p)$ was 0.005 mm (0.1 pixel multiplied by the magnification). Thus, the velocity uncertainty relative to the free stream velocity was no more than 1.3%.

2.2.4   Correction of the blocked velocity field

In the PIV measurement, part of the velocity field could not be obtained directly because of the blocking of the model to the light path. Weighed divergence correction scheme (WDCS) [25], which is a post-processing method based on mass conservation, was used in the process of obtaining complete time-averaged flow fields. The whole process is described below. Linear interpolation was used to obtain the missing velocity field preliminarily. Then an iteration, including WDCS and Gauss filter, was used to seek a velocity field constrained by the mass conversation near the interpolation data. Figure 5 shows the time-averaged streamlines and normalized time-averaged velocity $\left(u_{\text{mean}}^2 + v_{\text{mean}}^2\right)^{1/2} / U_\infty$ contours of the original measurement field and the corrected field, in which the dotted line indicates the corrected part of the flow field. In Figure 5 and other PIV measurement results below, u_{mean} denotes the mean streamwise velocity, whose direction is the same as the x-direction, while v_{mean} denotes the mean vertical velocity, the direction of which is the same as the y-direction, perpendicular to the free stream and points over the wing.

3   Deformation characteristics of actively controlled membrane wing

3.1   Deformation distribution

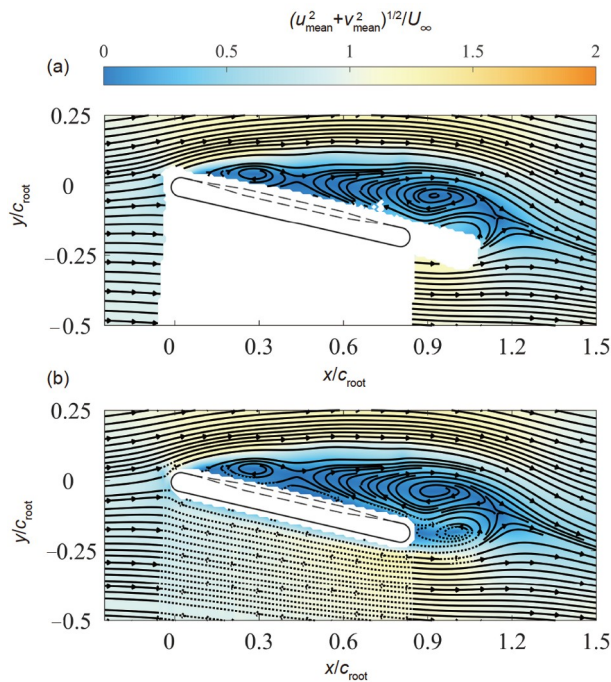The chordwise distribution of the deformation was measured

$(u_{mean}^2 + v_{mean}^2)^{1/2}/U_\infty$

Figure 5   (Color online) Correction of the velocity field (controlled wing at α=13°). (a) Original measurement field; (b) corrected field.
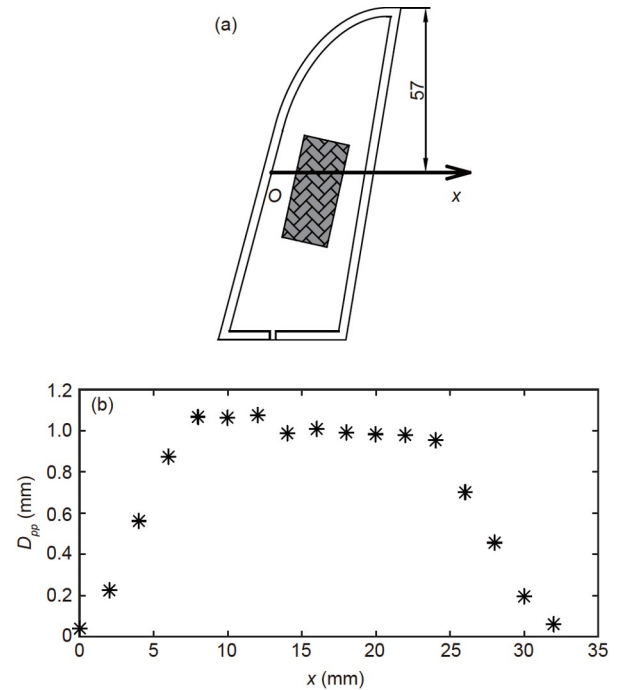

Figure 6   Chordwise distribution of the deformation. (a) Sketch of deformation measuring position; (b) peak-to-peak deformation along the wing chord line.
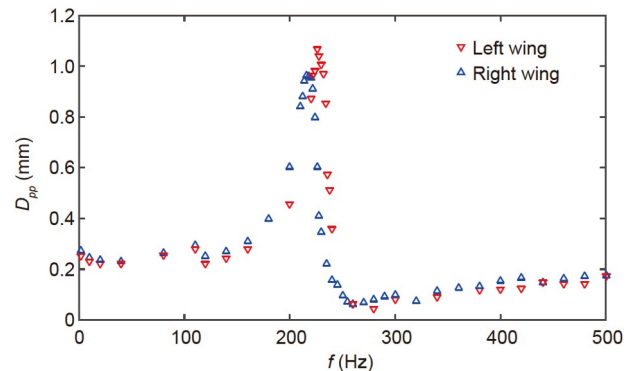
at the resonant frequency and maximum operating voltage of the MFC actuators (−500 V to 1500 V). The peak-to-peak displacements D_{pp} of several points on the mid-span chord line are shown in Figure 6. The spacing between the measured points is about 2 mm. It can be seen that the maximum vibration amplitude occurs on the actuator, reaching about 1 mm for the entire actuator.

3.2   Frequency characteristics of membrane deformation

The peak-to-peak displacements D_{pp} of the center position of the actuators on the left and right wings were measured at the maximum operating voltage and different frequencies. The results are shown in Figure 7.

It shows that actuation frequency has a considerable influence on membrane deformation. The resonance peak of each wing appears near 220 Hz with a maximum peak-to-peak displacement of about 1 mm as well as sharp drops before and after this frequency. While the minimum vibration amplitude occurs at around 260 Hz. Although there are slight differences between the left and right wings due to the manual operations in attaching the membrane and the actuators, the resonance frequencies of the two wings are coincident substantially. Both wings can achieve a peak-to-peak displacement of about 1 mm (about 2% of the length of the wing root) at the resonant frequency. Meanwhile, the resonant frequency of 220 Hz coincides with the structural frequency of the membrane with the actuator.

Figure 7   (Color online) Frequency characteristics of membrane deformation at V_{pp}=2000 V.

In addition, in the measurements, it is found that the morphing of the membrane is a sinusoidal vibration with the same frequency as the actuation signal, as shown in Figure 8 (the two signals were measured individually).

3.3   Variation of membrane deformation with voltage amplitude

The peak-to-peak displacements of the center position of the actuators on the left and right wings were measured at the resonant frequency (f=220 Hz) and different peak-to-peak voltages, as shown in Figure 8. It can be seen that the membrane deformation is proportional to the voltage amplitude.
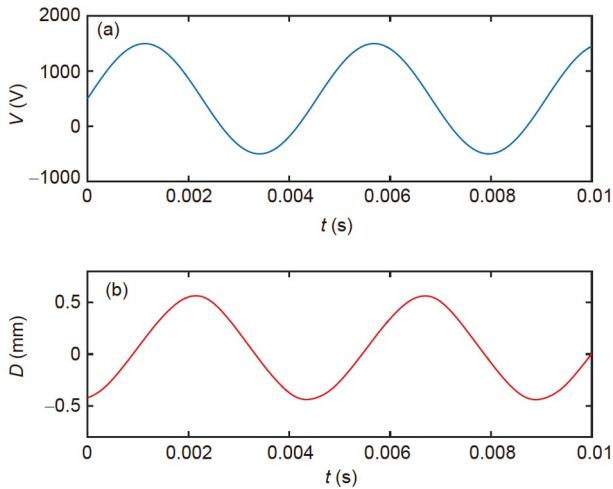
Figure 8 (Color online) Actuation signal and displacement signal at *f*=220 Hz and V_{pp}=2000 V. (a) Actuation signal *V*; (b) displacement signal *D* of the center position of the actuator on the left wing (pointing to the lower surface of the wing is positive).

4 Results and discussion

The influence and its mechanism of the membrane active deformation on the aerodynamic performance of the aircraft model was investigated based on the force and PIV measurements.

4.1 Aerodynamic performance

In this section, the aerodynamic forces of the controlled wing at the maximum operating voltage V_{pp}=2000 V and resonant frequency *f*=220 Hz, which has the optimal lift increment among all the actuation parameters in the experiment, are compared with the rigid wing, flexible wing, and uncontrolled wing, as shown in Figure 9.

Figure 9(a) shows the variation of lift coefficient with angle of attack. Two peaks are observed in all experimental models in the experimental range of *α*=0°–66°, which have been found and studied in previous works [15,26,27]. The first peak at stall angle of attack is more concerned in practice [28]. Compared with the rigid wing, the controlled wing has a remarkable effect on lift-enhancement in the range of *α*=7°–22°, and the stall angle of attack $α_s$ is delayed from 8° to 10°. Therefore, the corresponding lift coefficient C_{Ls} increase from 0.39 to 0.52 with an increment of 32.5%. Besides, the lift increment stabilizes at around 12% in the range of *α*=14°–19°, which had not been found in the investigation of periodic airfoil morphing carried out by Jones et al. [20]. In contrast, the lift increments of the flexible wing and the uncontrolled wing only appear in the range of *α*=7°–10°, and there is no significant delay for the stall angle of attack. This is consistent with a similar study by Acikel and Genc [29]. Meanwhile, the lift increment of the uncontrolled wing is slightly lower than the flexible wing, because of the
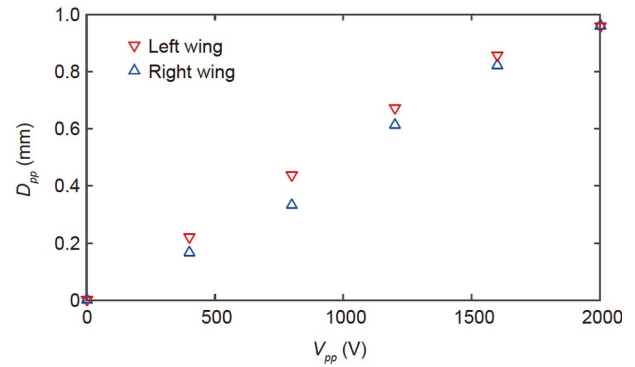

Figure 9 (Color online) Variation of membrane deformation with voltage amplitude (*f*=220 Hz).

effect of the actuator attaching to membrane deformation. Overall, it is indicated that the active deformation can improve aerodynamic performance more effectively.

Figure 9(b) shows the variation of drag coefficient with angle of attack. For further contrast, Figure 10 shows the drag coefficient increment ΔC_D of three types of wings compared with the rigid wing. Although the values of ΔC_D are partly impacted by the absolute uncertainty of the drag coefficient of about 0.006, the increment in drag can still be reflected and compared. It can be seen that both the drag coefficients of the controlled wing and flexible wing are increased, in which the controlled wing has a drag increment with a larger magnitude and a wider angle of attack range. However, the drag increment of the uncontrolled wing is not evident compared to the controlled wing and flexible wing. It indicates that both the active and passive deformation leads to drag increase, in which active deformation leads to greater drag as well as lift.

Figure 9(c) shows the variation of lift-to-drag ratio with the angle of attack. It can be seen that the controlled wing has a higher lift-to-drag ratio for *α*=8°–11° (near the stall angle, which is 8° and 10° for the rigid wing and the controlled wing, respectively), compared to the rigid wing and the uncontrolled wings. Besides, the maximum lift-to-drag ratio of the controlled wing, although slightly lower than that of the rigid wing and the uncontrolled wing, increases by 8.8% compared to the flexible wing. It is concluded that active deformation can increase the lift-to-drag ratio near the stall angle with a minor penalty of the maximum lift-to-drag ratio compared to the passive deformation case. Therefore, the application of active deformation near the stall angle of attack would be valuable in the improvement of the maneuverability of the aircraft.

In addition, the controlled wing exhibits hysteretic characteristics in the range of *α*=10°–17°, as shown in Figure 11.

Moreover, since the actuation parameters could significantly affect the deformation of the controlled wing (see Section 2.3), the aerodynamic forces of the controlled wing at other actuation parameters were also measured. Although
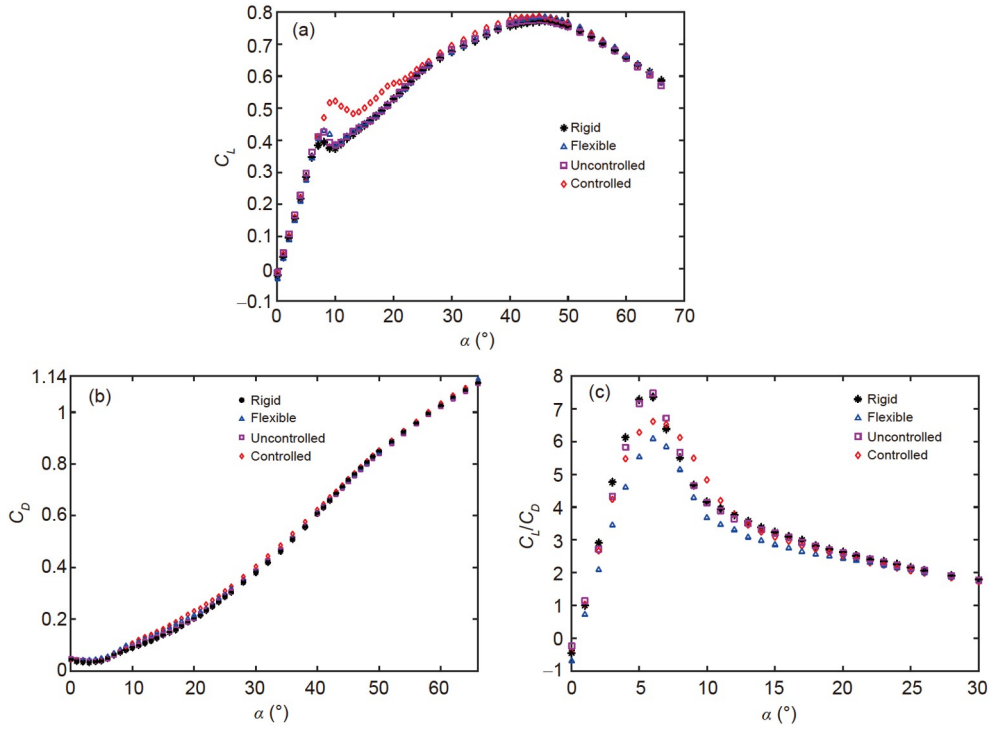
Figure 10 (Color online) Aerodynamic performance of four wings. (a) Lift coefficient; (b) drag coefficient; (c) lift-to-drag ratio ($\alpha=0°-30°$).
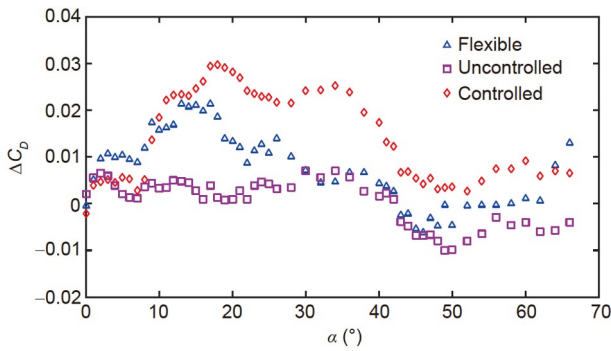

Figure 11 (Color online) Drag coefficient increment compared with the rigid wing.
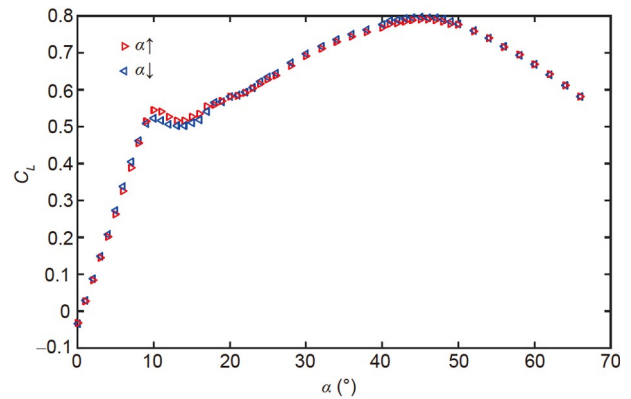

Figure 12 (Color online) Hysteretic characteristics of the controlled wing.

the lift coefficient of the tested aircraft model could be improved at each actuation parameter, there are significant differences in the magnitude of the lift increment. Figure 12(a) compares the relative lift increments at stall angle $\Delta C_{Ls}/C_{Ls0}$ (C_{Ls0} is the C_{Ls} of the uncontrolled wing) of the controlled wing at different actuation parameters. Among all the actuation parameters in the experiment, the controlled wing has the optimal lift increment at the maximum operating voltage V_{pp}=2000 V and resonant frequency f=220 Hz. Besides, Figure 12(b) further attempts to associate the lift increments with the deformation parameters, which are nondimensionalized as

$$f^{+} = f \cdot c_{\text{root}} / U_{\infty}, \tag{4}$$

$$\overline{D_{pp}}^{+} = \overline{D_{pp}} / c_{\text{root}}, \tag{5}$$

where $\overline{D_{pp}}$ is the average of the peak-to-peak displacements

of the left and right wings. For most of the results, there is a trend that the lift increments increase with $(f^{+})^{2} \cdot \overline{D_{pp}}^{+}$. For the two points deviating from the fitting curve, it may be due to the coupling of the actuation frequencies (160 Hz and 330 Hz) with the natural frequency of vortex shedding in the wake. A modified Strouhal number $St_{m} = fc\sin(\alpha) / U_{\infty}$ of vortex shedding based on the projection distance is about 0.15–0.20 [30]. In consideration of the thickness of the wing in this work, a modified Strouhal number based on the projection distance of the wing root is calculated as

$$St_{\text{mroot}} = f\left[(c_{\text{root}} - t)\sin(\alpha_s) + t\right] / U_{\infty}. \tag{6}$$

Thus, the actuation frequencies of 160 Hz and 330 Hz result in St_{mroot}=0.076 and 0.169, corresponding to the

sub-harmonic and the vortex shedding frequency, respectively.

4.2   Velocity field

To reveal the mechanism behind the aerodynamic performance improvement of the membrane active deformation, the velocity fields of four types of wings (the actuation parameters of the controlled wing were set as f=220 Hz and V_{pp}=2000 V) at α=8°, 10°, 16° were measured with PIV.

4.2.1   Flow statistical characteristics
Due to the low Reynolds number of Re_c=6.1×10⁴, the laminar boundary layer upon the rigid wing is prone to separation. While, the disturbance of membrane vibration can promote the transition from laminar to turbulent, thereby suppressing flow separation. Figure 13 shows the time-averaged velocity fields at α=10°, which is the stall angle of the controlled wing, and the corresponding lift increment compared with the rigid wing is the largest. It can be seen

that the flow separates completely for the rigid wing, the flexible wing, and the uncontrolled wing, without reattaching downstream. While, for the controlled wing, separated flow can still reattach to the trailing-edge, and meanwhile, the separation bubble is even smaller and closer to the leading-edge than that of the other three types of wings at the stall angle of α=8° (shown in Figure 14). Besides, both the streamlines and the vertical velocity v_{mean} distributions, shown in Figure 15(a), indicate a downward deflection of the wake caused by the active membrane deformation, which was inapparent in the investigation of aircraft model with membrane wings carried out by Guo et al. [15]. In addition, because of the suppression of the leading-edge separation and the facilitation of the reattachment, the streamwise velocity u_{mean} deficit of the controlled wing is reduced significantly, as shown in Figure 15(b), which is a major cause of the lift-drag ratio increment near the stall angle. Overall, both the active and passive membrane deformation can suppress the flow separation in the immediate vicinity of the stall. The controlled wing is the most efficient design for
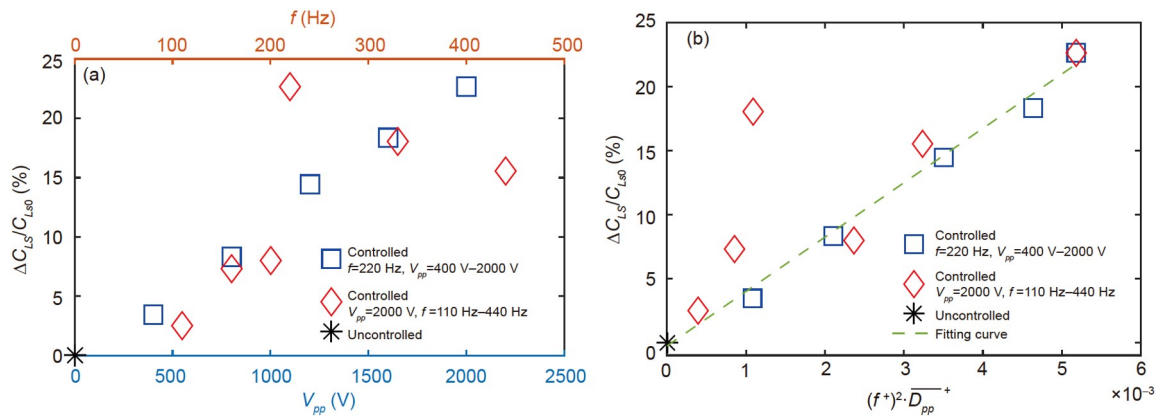

Figure 13   (Color online) Effects of the actuation parameters on lift increment. (a) Variation of lift increment with actuation parameters; (b) variation of lift increment with deformation parameters.
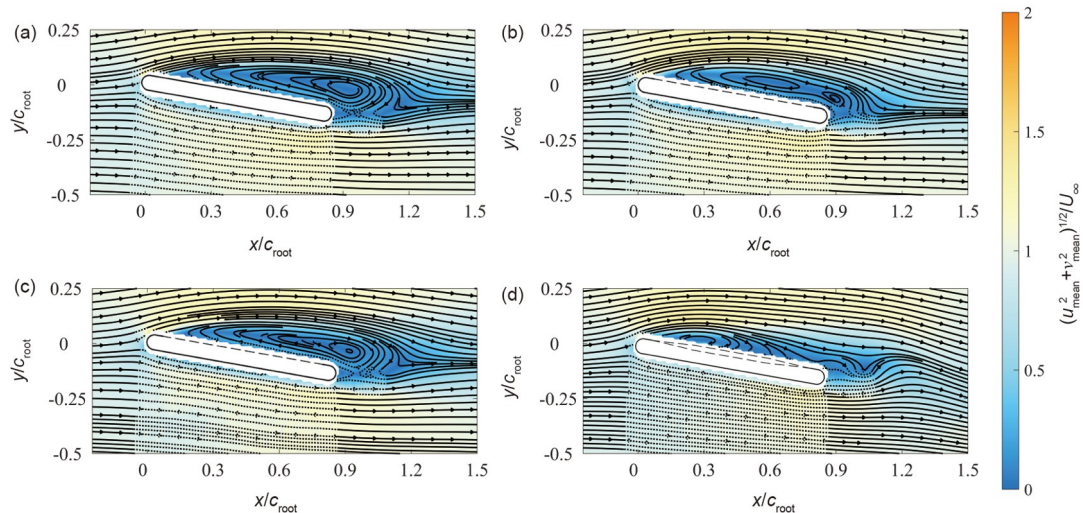

Figure 14   (Color online) Time-averaged velocity field at α=10°. (a) Rigid wing; (b) flexible wing; (c) uncontrolled wing; (d) controlled wing.

flow separation suppression, followed by the flexible wing, while the uncontrolled wing is the weakest. It is consistent with the results of force measurement.

Figure 16 shows the time-averaged velocity fields at $\alpha=16°$, corresponding to the stage where the controlled wing still has a lift increment after stall. Although the separated flow will not reattach downstream for both the rigid and controlled wing, the streamlines above the controlled wing have higher curvature and remarkable downward deflection, resulting in a much shorter separated bubble.

4.2.2   Turbulent characteristics

Figures 17 and 18 show the turbulent characteristics including turbulence kinetic energy $\overline{(u'^2+v'^2)} / U_\infty^2$ and Reynolds shear stress $\overline{u'v'} / U_\infty^2$ at $\alpha=10°$ and $16°$, respectively. The membrane active deformation changes the distribution of the turbulent kinetic energy and Reynolds shear stress remarkably. Higher turbulence kinetic energy and Reynolds shear stress are exhibited near the upper surface of the controlled wing. It indicates that membrane active deformation causes stronger flow mixing near the upper sur-

face, which provides energy for the reattachment or deflection of the separated boundary layer. Compare both wings at the stall angle ($\alpha=10°$ for the controlled wing and $\alpha=8°$ for the rigid wing shown in Figure 19), it can also be found that the turbulence kinetic energy and Reynolds shear stress near the leading-edge of the controlled wing are significantly enhanced. While the influence of membrane passive deformation on these turbulent characteristics is not obvious. Therefore, the results of the flexible and uncontrolled wing are not presented.

5   Conclusions

A simplified aircraft model with a pair of actively deformed membrane wings was adopted to investigate the influence of membrane active deformation. MFC actuators were used to control the membrane deformation. The results of deformation measurement show that the MFC actuator could effectively drive the entire membrane to produce active deformation. The maximum peak-to-peak deformation of 1 mm occurred at the resonant frequency of 220 Hz. Besides,
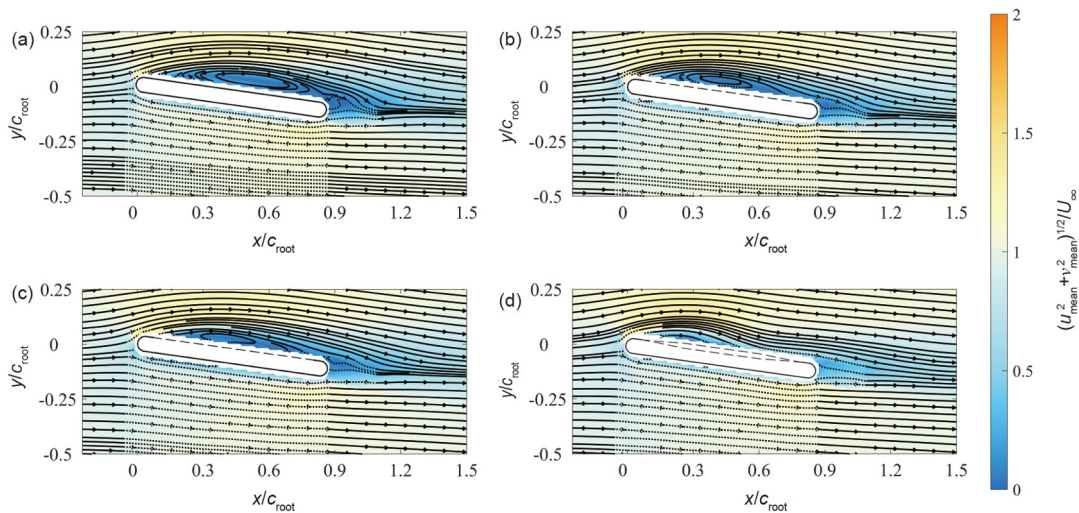

Figure 15 (Color online) Time-averaged velocity fields at $\alpha=8°$. (a) Rigid wing; (b) flexible wing; (c) uncontrolled wing; (d) controlled wing.
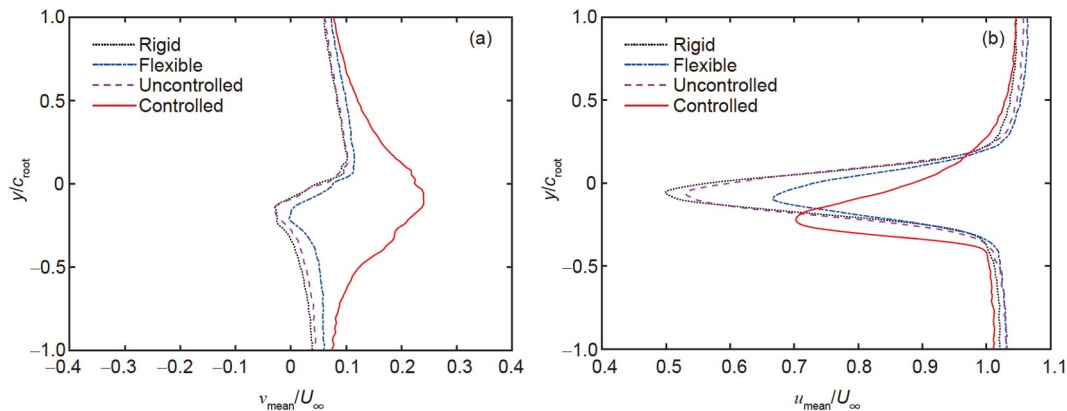

Figure 16 (Color online) Velocity distributions at $\alpha=10°$ ($x/c_{root}=1.5$). (a) Vertical velocity; (b) streamwise velocity.
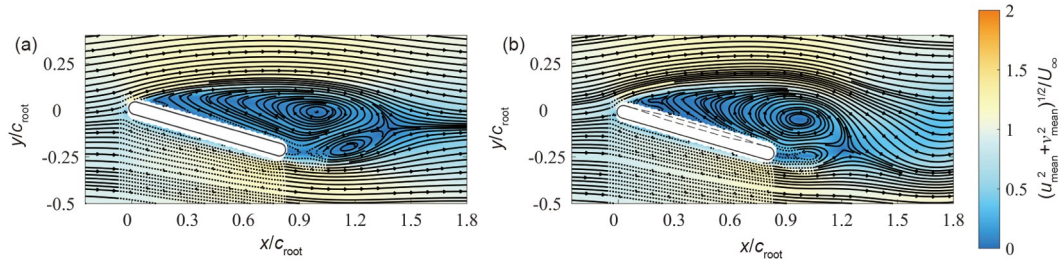
Figure 17 (Color online) Time-averaged velocity fields at $\alpha=16°$. (a) Rigid wing; (b) controlled wing.
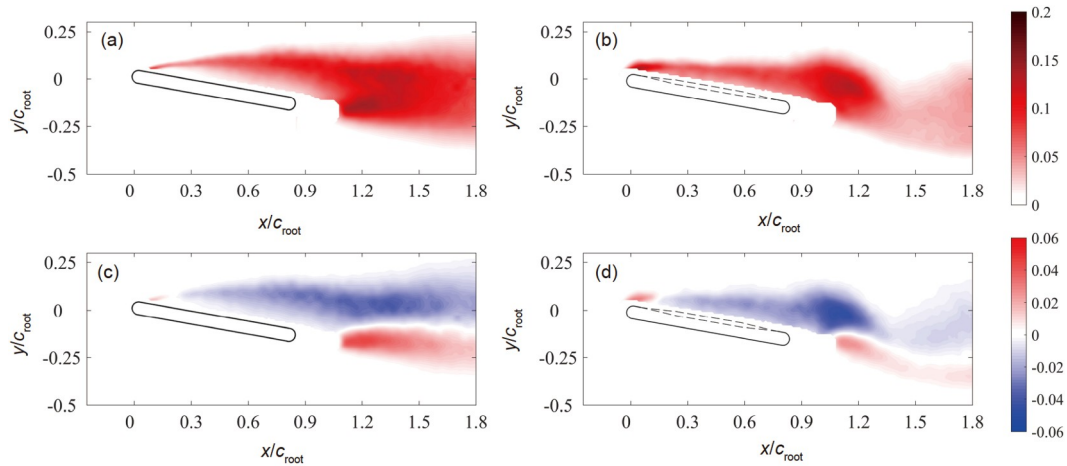

Figure 18 (Color online) Turbulent characteristics at $\alpha=10°$. (a) Rigid wing, turbulence kinetic energy; (b) controlled wing, turbulence kinetic energy; (c) rigid wing, Reynolds shear stress; (d) controlled wing, Reynolds shear stress.

Figure 19 (Color online) Turbulent characteristics at $\alpha=16°$. (a) Rigid wing, turbulence kinetic energy; (b) controlled wing, turbulence kinetic energy; (c) rigid wing, Reynolds shear stress; (d) controlled wing, Reynolds shear stress.
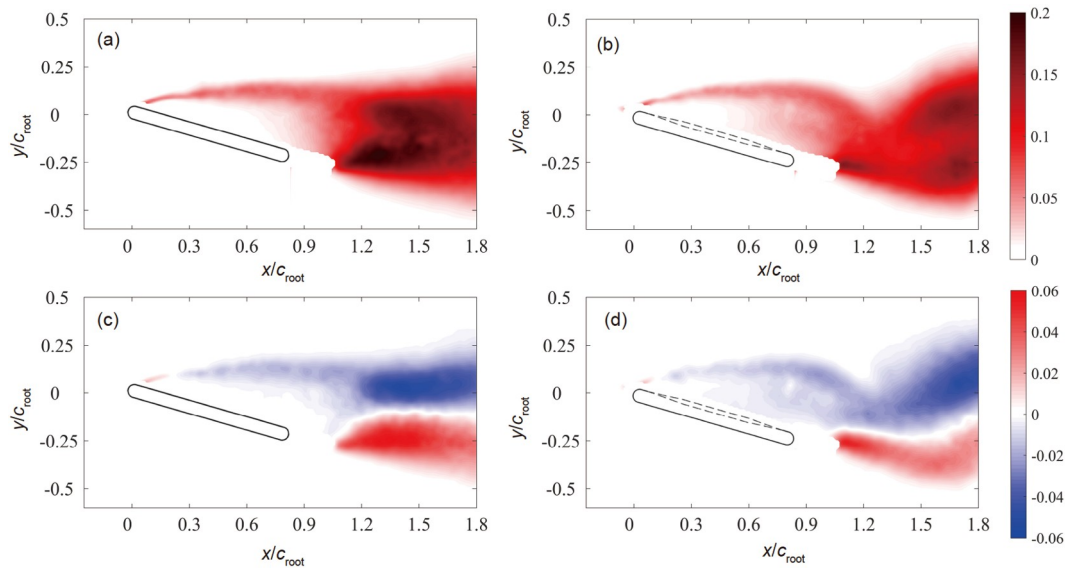
the peak-to-peak deformation was proportional to the voltage amplitude.

The wind tunnel experiment, including the force and flow field measurements, was conducted to evaluate the influence of the active deformation on aerodynamic performance. The main conclusions are as follows.

(1) The active deformation has a significant effect on lift enhancement and stall delay. In this investigation, the optimal control effect was obtained at the resonant frequency of 220 Hz and the maximum operating voltage of 2000 V.
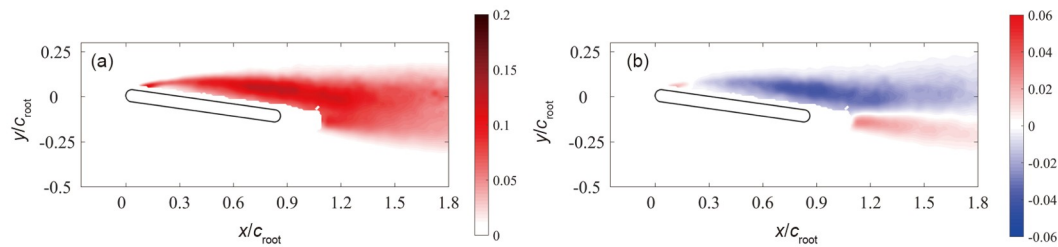
Figure 20 (Color online) Turbulent characteristics of the rigid wing at $\alpha=8°$. (a) Turbulence kinetic energy; (b) Reynolds shear stress.

Compared with the rigid wing, the lift of the controlled wing was increased remarkably in the range of $\alpha=7°-22°$. The stall angle was delayed by $2°$, and the relative lift coefficient was increased by 32.5%. This lift increment is much larger than the membrane passive deformation case.

(2) Compared with the passive deformation, the active deformation has a more powerful effect on suppressing the flow separation due to the stronger mixing near the upper wing surface. Moreover, the active deformed membrane wing can still increase lift by reducing the size of the separation bubble after stall.

In summary, this active control method using the high-frequency small-amplitude vibration of the membrane wing could obtain a considerable lift enhancement. Meanwhile, it just requires relatively small actuators compared with the entire wing (less than 15% in this work), as well as a relatively simple structure, which shows a great potential application in the design for future low Reynolds number aircraft.

1 Michelson R C. Overview of micro air vehicle system design and integration issues. In: Blockley R, Shyy W, eds. Encyclopedia of Aerospace Engineering. New Jersey: John Wiley & Sons, Ltd, 2010

2 Shyy W, Ifju P, Viieru D. Membrane wing-based micro air vehicles. Appl Mech Rev, 2005, 58: 283–301

3 Levin O, Shyy W. Optimization of a low Reynolds number airfoil with flexible membrane. Cmes-Comp Model Eng, 2001, 2: 523–536

4 Smith R, Shyy W. Computational model of flexible membrane wings in steady laminar flow. AIAA J, 1995, 33: 1769–1777

5 Smith R, Shyy W. Computation of unsteady laminar flow over a flexible two-dimensional membrane wing. Phys Fluids, 1995, 7: 2175–2184

6 Ifju P G, Jenkins D A, Ettinger S, et al. Flexible-wing-based micro air vehicles. In: 40th AIAA Aerospace Sciences Meeting & Exhibit. Reno, Nevada, 2002

7 Rojratsirikul P, Wang Z, Gursul I. Effect of pre-strain and excess length on unsteady fluid-structure interactions of membrane airfoils. J Fluids Struct, 2010, 26: 359–376

8 Huang G, Xia Y, Dai Y, et al. Fluid-structure interaction in piezo-electric energy harvesting of a membrane wing. Phys Fluids, 2021, 33: 063610

9 Song A, Tian X, Israeli E, et al. Aeromechanics of membrane wings with implications for animal flight. AIAA J, 2008, 46: 2096–2106

10 Rojratsirikul P, Wang Z, Gursul I. Unsteady fluid-structure interactions of membrane airfoils at low Reynolds numbers. Exp Fluids,

2009, 46: 859–872

11 He X, Wang J J. Fluid–structure interaction of a flexible membrane wing at a fixed angle of attack. Phys Fluids, 2020, 32: 127102

12 Bleischwitz R, de Kat R, Ganapathisubramani B. Aspect-ratio effects on aeromechanics of membrane wings at moderate Reynolds numbers. AIAA J, 2015, 53: 780–788

13 Béguin B, Breitsamter C, Adams N. Aerodynamic investigations of a morphing membrane wing. AIAA J, 2012, 50: 2588–2599

14 Béguin B, Breitsamter C. Effects of membrane pre-stress on the aerodynamic characteristics of an elasto-flexible morphing wing. Aerospace Sci Tech, 2014, 37: 138–150

15 Guo Q, He X, Wang Z, et al. Effects of wing flexibility on aero-dynamic performance of an aircraft model. Chin J Aeronautics, 2021, 34: 133–142

16 Hays M R, Morton J, Dickinson B, et al. Aerodynamic control of micro air vehicle wings using electroactive membranes. J Intelligent Material Syst Struct, 2012, 24: 862–878

17 Curet O M, Carrere A, Waldman R, et al. Aerodynamic character-ization of a wing membrane with variable compliance. AIAA J, 2014, 52: 1749–1756

18 Bohnker J R, Breuer K S. Control of separated flow using actuated compliant membrane wings. AIAA J, 2019, 57: 3801–3811

19 Bouremel Y, Chan W L, Jones G, et al. Measurements of a symmetric airfoil morphed by macro fiber composite actuators. In: 32nd AIAA Applied Aerodynamics Conference. Atlanta, Georgia, 2014

20 Jones G R, Debiasi M, Bouremel Y, et al. Open-loop flow control at low Reynolds numbers using periodic airfoil morphing. In: 53rd AIAA Aerospace Sciences Meeting. Kissimmee, Florida, 2015

21 Wang J J, Liu Y. Experimental study on lift characteristics for flow over flexible cropped delta wings. J Aircraft, 2008, 45: 2158–2161

22 Zhan J X, Wang J J. The effect of leading-edge sweep angle asymmetry on lateral aerodynamics. Sci China Ser E-Technol Sci, 2009, 52: 2445–2448

23 Qu Y, Wang J, Feng L, et al. Effect of excitation frequency on flow characteristics around a square cylinder with a synthetic jet positioned at front surface. J Fluid Mech, 2019, 880: 764–798

24 Kline S J, McClintock F A. Describing uncertainties in single-sample experiments. Mech Eng, 1953, 75: 3–8

25 Wang C Y, Gao Q, Wei R J, et al. Weighted divergence correction scheme and its fast implementation. Exp Fluids, 2017, 58: 44

26 Michos A, Bergeles G, Athanassiadis N. Aerodynamic characteristics of NACA 0012 airfoil in relation to wind generators. Wind Eng, 1983, 7: 247–262

27 Zhou Y, Alam M M, Yang H X, et al. Fluid forces on a very low Reynolds number airfoil and their prediction. Int J Heat Fluid Flow, 2011, 32: 329–339

28 Marchman J F. Aerodynamic testing at low Reynolds numbers. J Aircraft, 1987, 24: 107–114

29 Acikel H H, Genc M S. Control of laminar separation bubble over wind turbine airfoil using partial flexibility on suction surface. Energy, 2018, 165: 176–190

30 Rojratsirikul P, Genc M S, Wang Z, et al. Flow-induced vibrations of low aspect ratio rectangular membrane wings. J Fluids Struct, 2011, 27: 1296–1309